





Reversible transition between the polar and antipolar phases and its implications for wake-up and fatigue in HfO₂-based ferroelectric thin film

Yan Cheng^{1,8}, Zhaomeng Gao^{2,3,8}, Kun Hee Ye^{4,5}, Hyeon Woo Park⁴, Yonghui Zheng¹, Yunzhe Zheng¹, Jianfeng Gao², Min Hyuk Park^{4,6}, Jung-Hae Choi ⁵, Kan-Hao Xue ⁷, Cheol Seong Hwang ⁴✉ & Hangbing Lyu ^{2,3}✉

Atomic-resolution Cs-corrected scanning transmission electron microscopy revealed local shifting of two oxygen positions (O_I and O_{II}) within the unit cells of a ferroelectric (Hf_{0.5}Zr_{0.5})O₂ thin film. A reversible transition between the polar *Pbc2₁* and antipolar *Pbca* phases, where the crystal structures of the 180° domain wall of the *Pbc2₁* phase and the unit cell structure of the *Pbca* phase were identical, was induced by applying appropriate cycling voltages. The critical field strength that determined whether the film would be woken up or fatigued was ~0.8 MV/cm, above or below which wake-up or fatigue was observed, respectively. Repeated cycling with sufficiently high voltages led to development of the interfacial nonpolar *P4₂/nmc* phase, which induced fatigue through the depolarizing field effect. The fatigued film could be rejuvenated by applying a slightly higher voltage, indicating that these transitions were reversible. These mechanisms are radically different from those of conventional ferroelectrics.

¹Key Laboratory of Polar Materials and Devices (MOE), Department of Electronics, East China Normal University, 500 Dongchuan Road, 200241 Shanghai, China. ²Key Laboratory of Microelectronics Devices and Integrated Technology, Institute of Microelectronics, Chinese Academy of Sciences, No. 3 Bei-tu-cheng West Road, Chaoyang District, 100029 Beijing, China. ³University of Chinese Academy of Sciences, 100049 Beijing, China. ⁴Department of Materials Science and Engineering, and Inter-University Semiconductor Research Center, College of Engineering, Seoul National University, 08826 Seoul, Republic of Korea. ⁵Electronic Materials Research Center, Korea Institute of Science and Technology, 02792 Seoul, Republic of Korea. ⁶School of Materials Science and Engineering, College of Engineering, Pusan National University, Busandaehak-ro 63beon-gil 2, Geumjeong-gu, 46241 Busan, Republic of Korea. ⁷Wuhan National Laboratory for Optoelectronics, School of Optical and Electronic Information, Huazhong University of Science and Technology, 430074 Wuhan, China. ⁸These authors contributed equally: Yan Cheng, Zhaomeng Gao. ✉email: cheolsh@snu.ac.kr; lvhangbing@ime.ac.cn

Ensuring reliable and repeatable electrical performance from ferroelectric (FE) thin films and devices present a significant challenge for conventional FE materials such as perovskite-structured $\text{Pb}(\text{Zr},\text{Ti})\text{O}_3$ (PZT) to enable their use in FE memory devices^{1–4}. Among the potential problems, fatigue, which is induced by defect (mainly oxygen vacancy (V_{O})) generation⁵ and the accompanying FE domain pinning^{6,7} that occurs during repeated electrical stimulation, is one of the most critical concerns^{1–4}. While the discovery of ferroelectricity in doped HfO_2 thin films by Böske et al.⁸ in 2011 has again triggered enormous interest in FE memories^{2–4} and several other novel applications^{1,9–11}, these films are not exempt from serious fatigue concerns^{2,3}. However, the much higher binding energy of the Hf–O bond when compared with the Ti–O bond in PZT makes serious V_{O} involvement in the fatigue in this material unlikely.

Another interesting but also undesirable effect in this new FE material is wake-up (a temporal increase in the switchable polarization during the first 10^4 – 10^5 switching cycles)^{12–16}. This has been ascribed to the decrease in the non-ferroelectric tetragonal interfacial layer (T-phase, $P4_2/nmc$) caused by the reduced V_{O} concentration in the layer^{13,15}. However, a reactive TiN electrode would be likely to increase the V_{O} concentration during repeated cycling^{13,15}. Therefore, these two issues, i.e., severe fatigue and wake-up, as direct consequences of the V_{O} effect are hardly understood.

In fluorite-structured FE materials, four of the eight oxygen ions within each unit cell were shifted along the c axis direction (O_{II} ions), while the other four oxygen ions (O_{I} ions) remained in centrosymmetric positions^{17,18}. The energy of the polar phase (FE $Pca2_1$, where all O_{II} ions shift in the same direction) is only slightly higher than that of the antipolar phase (antiferroelectric (AFE) $Pbca$, where O_{II} ions shift into antiparallel directions) by ~ 10 meV/f.u.^{17,19}. These specific crystallographic features of HfO_2 -based FE materials may render the transition between the FE $Pca2_1$ and AFE $Pbca$ phases to be both fluent and reversible, depending on the bias voltage conditions, and maybe the origin of the fatigue and wake-up phenomena. However, this probability has scarcely been examined to date.

This work used an advanced imaging technique, Cs-corrected scanning transmission electron microscopy in annular bright-field mode (STEM-ABF), which enables reliable imaging of light atomic columns (oxygen) in the presence of much heavier atomic columns (Hf and Zr) in fluorite-structured ($\text{Hf}_{0.5}\text{Zr}_{0.5}$) O_2 (HZO) films²⁰. The pristine, woken-up, fatigued, and rejuvenated 10- to 15-nm-thick HZO films were prepared by electrical cycling of TiN/HZO/TiN FE capacitors. The atomistic structural evolutions

occurring in each state were examined using the STEM-ABF technique. The involvement of V_{O} effect was observed during fatigue cycling, which increased the interfacial T-phase, but the direct cause of the fatigue differed fundamentally from that in conventional FE materials. The wake-up, fatigue, and rejuvenation were mediated by the (reversible) transition between the FE $Pca2_1$ and AFE $Pbca$ phases. This conclusion was further supported by theoretical calculations based on density functional theory (DFT). The theoretical findings on the switching path and the bias voltage dependence matched the experimental results very well.

Results

A TiN/HZO/TiN capacitor with HZO thickness of 15 nm was fabricated using the atomic layer deposition (ALD) process at a substrate temperature of 280 °C (see “Methods” section). Because the FE orthorhombic phase (O_{FE} -phase, $Pca2_1$) is not the thermodynamically stable bulk phase^{21,22}, it could be achieved by kinetic means, supplemented by the surface energy/stress effects in the fine-grained (~ 10 nm) polycrystalline thin films^{17,23}. This phase formation could be enabled by a specific kinetic phase transition from the amorphous as-deposited ALD material during post-deposition annealing (PDA)^{24–26}. The typical thickness of the HZO film with the highest remanent polarization (P_{r}) was ~ 10 nm, but a slightly greater thickness (15 nm) was used in this work to ease the STEM characterization.

Figure 1a shows the cross-section of the pristine (before electrical cycling) TiN/HZO/TiN structure, which was observed by STEM in the high-angle annular dark-field (HAADF) mode. In the figure, one of the grains in the HZO film that penetrates through the entire film thickness was identified. The bright contrast region corresponds to the Hf and Zr ionic columns, which confirmed that the grain’s crystal structure is O-phase. However, the different space groups (SGs) among the various O phases cannot be identified by recognition of heavy Hf/Zr ions alone. In particular, identification of the O_{FE} -phase $Pca2_1$ (SG: 29) and the antipolar O_{AFE} -phase $Pbca$ (SG: 61) is an advantage of the STEM-ABF technique, which has a high sensitivity to light elements, i.e., oxygen ions. Zooming in to the dashed green square area in Fig. 1a in STEM-ABF mode allowed the oxygen ion positions to be determined clearly, as shown in Fig. 1b. Using the shifts in the oxygen ion positions from the centers of the four nearest Hf/Zr ion positions, the oxygen ions can be divided into O_{I} -type (navy blue, at the centrosymmetric position) and O_{II} -type (cyan, at the off-center position). Here, for ease of comparison of the two crystal structures, the polar O_{FE} -phase was identified as

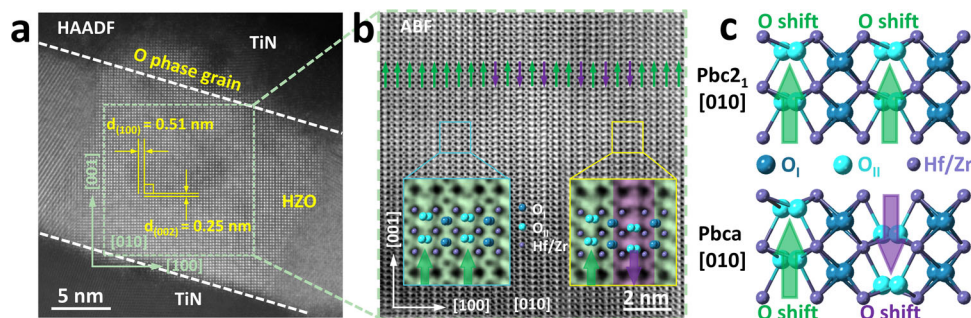


Fig. 1 The observation of oxygen atoms of single orthorhombic (O-) phase grain in pristine TiN/ $\text{Hf}_{0.5}\text{Zr}_{0.5}\text{O}_2$ (HZO, 15 nm)/TiN device. **a** Scanning transmission electron microscopy (STEM) high-angle annular dark-field (HAADF) image of the TiN/HZO/TiN cross-section. **b** Annular bright-field (ABF) image extracted from the green square area in **a**, in which the position of the O atomic columns can be clearly detected with different offset and direction. According to the O atomic columns deviated from the center of the four nearest Hf/Zr columns, it can be divided into O_{I} type (center) and O_{II} type (off-center). Some of the O_{II} -site columns shift along the [001], while others shift to the opposite direction. **c** The atomic models of the $Pbc2_1$ and $Pbca$ phases along [010] direction. The purple, navy blue, and cyan-colored solid balls correspond to the Hf/Zr, O_{I} (center), and O_{II} (off-center) ions, respectively.

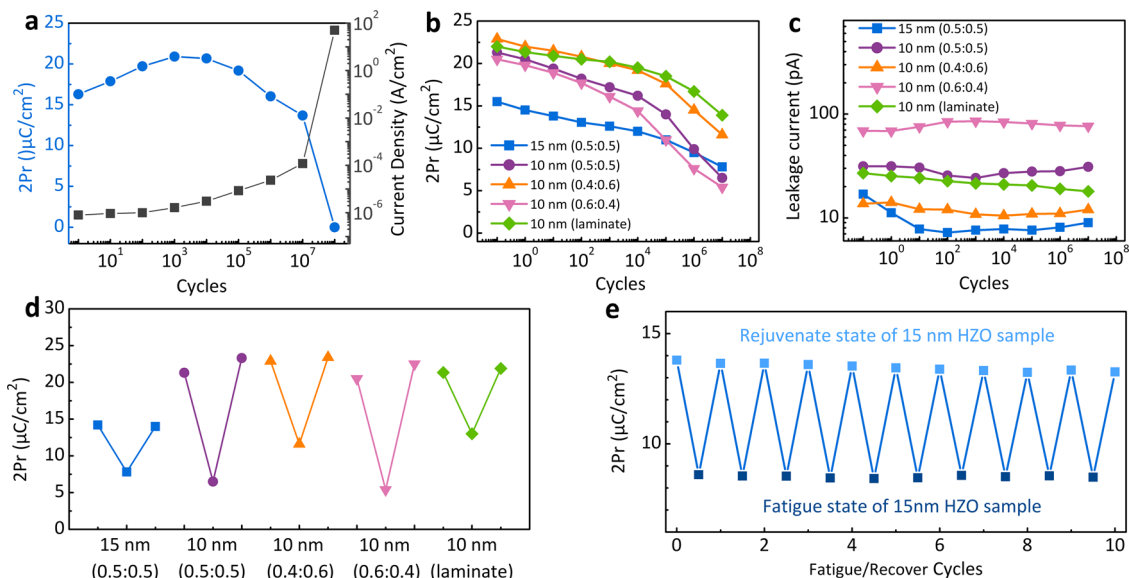


Fig. 2 Electrical measurement results of different TiN/HZO/TiN devices: 15-nm-thick $\text{Hf}_{0.5}\text{Zr}_{0.5}\text{O}_2$, 10-nm-thick $\text{Hf}_{0.5}\text{Zr}_{0.5}\text{O}_2$, 10-nm-thick $\text{Hf}_{0.4}\text{Zr}_{0.6}\text{O}_2$, 10-nm-thick $\text{Hf}_{0.6}\text{Zr}_{0.4}\text{O}_2$, and the nanolaminated 10-nm-thick $\text{Hf}_{0.5}\text{Zr}_{0.5}\text{O}_2$ films. **a** The $2P_r$ of 15-nm-thick $\text{Hf}_{0.5}\text{Zr}_{0.5}\text{O}_2$ device measured by ± 3 V P - V loop and the corresponding leakage currents measured at 2 V, as a function of switching cycles, which was performed by applying bipolar voltage pulses of ± 5 V at $f = 500$ kHz. **b** The trend of $2P_r$ changes of different devices with the switching cycles at a low field of ± 1.8 MV/cm. **c** The corresponding leakage current changes with the cycles. **d** The rejuvenation process of different devices by applying field pulses of ± 3 MV/cm. **e** Ten cycles of fatigue/rejuvenation process on the 15-nm-thick $\text{Hf}_{0.5}\text{Zr}_{0.5}\text{O}_2$ device under ± 2.2 V, 5×10^6 bipolar pulses for fatigue and ± 4.0 V, 1×10^4 bipolar pulses for recovery.

the Pbc_2_1 phase rather than the standard Pca_2_1 , which causes the a -, b -, and c axis directions of the two O-phases to coincide. There are two shift directions for the O_{II} -type ions: along the $[001]$ direction (green arrows; majority of O_{II} ions) and along the $[00\bar{1}]$ direction (purple arrow; minority of O_{II} ions). Note that atomic-resolution TEM images show the projected positions of atoms along the beam direction (in this case, the $[010]$ O-phase direction). If mixtures of O_I and O_{II} positions were present along this direction, there could hardly be a clear distinction between the O_I and O_{II} positions in the STEM-ABF image, but this was not the case (see the enlarged images in the insets). Therefore, there are two types of crystal region: one with all O_{II} ions shifting along the $[001]$ direction (green arrows) and another with O_{II} ions shifting alternately along the $[001]$ and $[00\bar{1}]$ directions (purple and green arrows, respectively), which can be identified more clearly in the enlarged insert images from Fig. 1b. The larger proportion with green arrows corresponds to the Pbc_2_1 O_{FE} domain with uniform polarization (P). The regions with alternating green- and purple-colored arrows might be regarded as the Pbc_2_1 O_{FE} -phase with a one-unit-cell-thick FE domain width, but an even more appropriate interpretation would be that it is the O_{AFE} $Pbca$ phase. Figure 1c exhibits the two kinds of atomic models of the Pbc_2_1 and $Pbca$ phases along $[010]$ direction, in which the purple, navy blue, and cyan-colored solid balls correspond to the Hf/Zr, O_I (center), and O_{II} (off-center) ions, respectively. A detailed atomic structure comparison of the O_{FE} Pbc_2_1 and O_{AFE} $Pbca$ phases is shown in Supplementary Fig. S1, which contains self-consistent experimental and theoretical ABF images. These results indicate that many of the O-phase single grains in the pristine state are composed of a mixture of the O_{FE} Pbc_2_1 and O_{AFE} $Pbca$ phases. This is expected because the free energies of these two phases are quite similar, and the crystallization stage during PDA processing thus involved a high probability of formation of these structures.

It is commonly believed that the hafnia-based ferroelectric capacitors undergo a wake-up-fatigue-breakdown trend under

continuous switching cycles. Figure 2a shows the variations in $2P_r$ and the leakage currents of a TiN/ $\text{Hf}_{0.5}\text{Zr}_{0.5}\text{O}_2$ (15 nm)/TiN capacitor with increasing numbers of switching cycles (bipolar voltage pulses of ± 5 V at $f = 500$ kHz). The $2P_r$ was measured by ± 3 V P - V loop, and the leakage current was measured at 2 V. During the first 10^4 cycles, wake-up occurs, and the leakage current remains almost constant. During subsequent cycling up to $\sim 10^7$ cycles, the samples showed gradual fatigue (with $2P_r$ decreasing from ~ 20.7 to 13.7 $\mu\text{C}/\text{cm}^2$) and a simultaneous increase in the leakage current by more than 50 times. The sample broke down completely after 10^8 cycles. The field-dependent wake-up process was shown in Supplementary Fig. S2 (for the 15 nm $\text{Hf}_{0.5}\text{Zr}_{0.5}\text{O}_2$ film), where all $2P_r$ values were measured using a ± 3 V P - V loop after each decade of cycles. At low voltages (< 3.2 V), no obvious wake-up was observed, but the $2P_r$ value decreased monotonically with increasing numbers of switching cycles. However, at $V_a > 3.6$ V, wake-up was clearly observed. Figure 2b shows the $2P_r$ evolution of samples with 15-nm-thick $\text{Hf}_{0.5}\text{Zr}_{0.5}\text{O}_2$, 10-nm-thick $\text{Hf}_{0.6}\text{Zr}_{0.4}\text{O}_2$, 10-nm-thick $\text{Hf}_{0.5}\text{Zr}_{0.5}\text{O}_2$, 10-nm-thick $\text{Hf}_{0.4}\text{Zr}_{0.6}\text{O}_2$, and the nanolaminated 10-nm-thick $\text{Hf}_{0.5}\text{Zr}_{0.5}\text{O}_2$ films, under bipolar V_a pulses of ± 1.8 MV/cm, which are lower than the critical wake-up field (Supplementary Fig. S3). The $2P_r$ values remained relatively constant up to $\sim 10^4$ cycles and decreased rapidly toward much smaller values at 10^7 cycles. The capacitor leakage currents were also measured at each decade of low-field cycling pulses, but no obvious increase in leakage current was observed, as shown in Fig. 2c. These findings indicated that the fatigue caused by low V_a values is irrelevant to the generation of new defects. Figure 2d shows the low- V_a fatigue and subsequent rejuvenation process. After the devices were fatigued using bipolar ± 1.8 MV/cm, 10^7 pulse cycles, and then rejuvenated by subsequent application of ± 3 MV/cm, 10^4 recovery pulse cycles. The rejuvenated capacitor could be fatigued and rejuvenated again, with ten cycles of repetitive fatigue/recovery process, as shown in Fig. 2e. This “temporary” low- V_a fatigue and rejuvenation phenomenon is

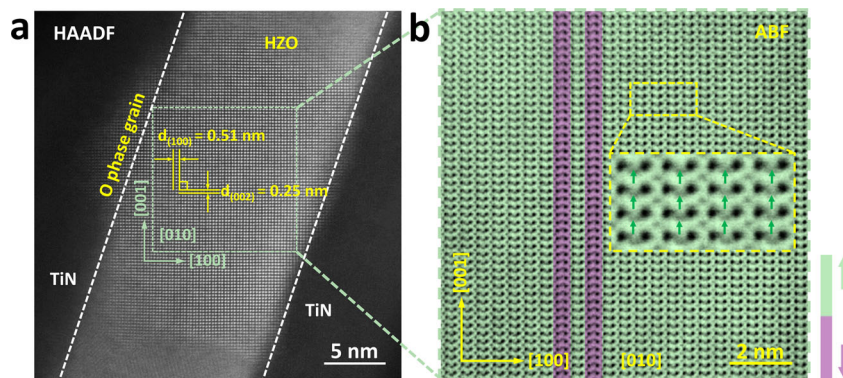


Fig. 3 The observation of O_{AFE} $Pbca$ phase returning to O_{FE} $Pbc2_1$ phase after wake-up process. **a** Cross-section STEM-HAADF image of the TiN/HZO/TiN device after wake-up under the bipolar triangle pulses of ± 4 V, 10^4 cycles with $f = 500$ kHz, in which a [010] oriented HZO O-phase grain is examined. **b** ABF image acquired from the green square area in **a**, the majority of the off-center O_{II} atomic columns shifted along the [001] direction (green), demonstrating a $Pbc2_1$ -dominated phase structure after the wake-up. The inset magnified ABF image shows the shifting direction of O_{II} atomic columns deviating from the center of the four nearest Hf/Zr columns, fitting well with $Pbc2_1$ structure.

quite different from the conventional perception of fatigue, which is generally regarded as an irrecoverable process that causes permanent P_r degradation and device failure^{15,27,28}. These findings indicate that the changes in the internal (defect) structure of the HZO film during field cycling are different for the low and high V_a values. In the low- V_a cycling case, the main fatigue mechanism is probably the phase transition from the O_{FE} $Pbc2_1$ to the O_{AFE} $Pbca$ phase, while the rejuvenation can be ascribed to the reverse phase transition without involving permanent structural change or V_O generation. In contrast, the changes shown during high- V_a cycling may involve a specific permanent structural change, e.g., V_O generation and an accompanying phase transition. The subsequent STEM-ABF observations of the woken-up, fatigued, and rejuvenated samples confirmed the above hypotheses.

Figure 3a shows a STEM-HAADF image of the woken-up sample, which was cycled 10^4 times at $V_a = \pm 4$ V and $f = 500$ kHz to wake-up the sample effectively but minimize the damaging effects of defect generation. The image shows an O_{FE} - or O_{AFE} -phase grain projected along the [010] zone axes. The corresponding STEM-ABF image is shown in Fig. 3b, in which the oxygen ion locations can be observed clearly. The image shows that most of the O_{II} atomic columns shift along the [001] direction (green), with only two vertical O_{II} columns with the opposite shift (purple) remaining; this indicates that almost the entire film becomes the O_{FE} $Pbc2_1$ phase. The inset image in Fig. 3b shows a close-up that clearly reveals that all the O_{II} ions shifted in the same direction. Therefore, the wake-up effect could be correlated positively with the structural transition from the O_{AFE} -phase in the pristine sample to the O_{FE} -phase after cycling. This is a distinctive interpretation of the wake-up effect in this material when compared with the previous interpretation, which described it as the result of V_O redistribution from the interfacial nonpolar T-phase into the interior part of the O_{FE} -phase film¹⁵. However, STEM observation of the interfacial region near the top electrode across the broad areas of both the pristine and woken-up samples (Supplementary Fig. S4a, b) showed that the interfacial T-phase thickness actually increased slightly, from 0.75–1.0 nm (pristine state) to 0.94–2.11 nm (woken-up state). This indicates that the interfacial nonpolar T-phase to O_{FE} -phase transition may not be the major mechanism of the wake-up process. In contrast, the interpretation of the wake-up effect based on the O_{AFE} -phase to O_{FE} -phase transition in the bulk thin-film region does not involve such a difficulty. Additionally, it is consistent with the non-varying leakage current observed during the wake-up process (Supplementary Fig. S2).

The same reasoning implies that fatigue could also be induced by the reverse transition, i.e., from the O_{FE} $Pbc2_1$ phase in the pristine state to the O_{AFE} $Pbca$ phase after the fatigue. To confirm this hypothesis, a pristine 15-nm-thick $Hf_{0.5}Zr_{0.5}O_2$ film was cycled 10^6 times at $V_a = \pm 2.5$ V and $f = 500$ kHz, which corresponds to low- V_a fatigue without involving an intermediate wake-up. This cycling operation reduced the $2P_r$ value from ~ 9.4 to ~ 2.0 $\mu C/cm^2$ (read at ± 2.5 V, data not shown here). Figure 4a, b shows STEM-HAADF and STEM-ABF images of such a low- V_a fatigued sample, respectively. The images demonstrate that almost the entire area of the film was now in the O_{AFE} -phase, which was further confirmed by the magnified view shown in Fig. 4c. To further verify the validity of the antipolar-polar transition model, the crystalline structure of other devices were examined at the low field fatigued and woken-up states, respectively. Supplementary Figs. S5–6 show the STEM-HAADF and STEM-ABF cross-section images of the 10-nm-thick nanolaminated $Hf_{0.5}Zr_{0.5}O_2$ film. They also show a clear $Pbca$ phase structure after the low-field fatigue and $Pbc2_1$ phase-dominated structure after the wake-up. Similarly, Supplementary Figs. S7 and 8 show the reversible transition between the antipolar $Pbca$ and polar $Pbc2_1$ phases as the origin of the low-field fatigue and rejuvenation in the 10-nm-thick $Hf_{0.5}Zr_{0.5}O_2$ film. As discussed below, the O_{AFE} -phase free energy is lower than that of the O_{FE} -phase by ~ 10 meV/f.u., thus indicating that this transition is energetically favorably driven. It was noted that the low- V_a fatigue only occurred with bipolar switching pulses. Stressing the device using unipolar voltages of the same amplitude did not cause fatigue (see Supplementary Fig. S9 and related discussion).

The question then becomes this: what is the critical field strength that determines whether fatigue or wake-up (and also rejuvenation) will occur? To answer this question, DFT was used to simulate the switching path from the $Pbca$ global minimum energy phase to the $Pbc2_1$ local minimum energy phase. Details of the calculations are included in SM (Supplementary Fig. S10). The effective electric field (E_{eff}) distribution across the O_{FE} region of the film, which must be smaller than the applied field (E_{app}) because of the presence of the non-FE layer, was also calculated by assuming the presence of the interfacial T-phase based on the STEM results (Supplementary Fig. S11). The presence of non-polar layers in series with the FE film induces the depolarization field, which reduces the effective field greatly during the switching cycles. The goal of these calculations is to estimate the critical field (E_0) that can make the polar O_{FE} phase more stable than the O_{AFE} phase by its electrostatic energy contribution.

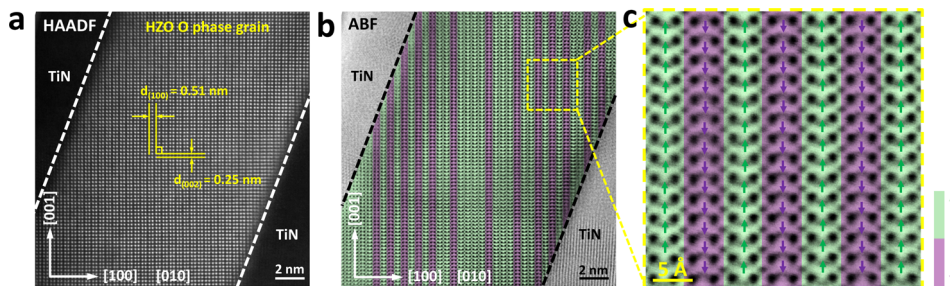


Fig. 4 Phase transition from $O_{FE} Pbc2_1$ to $O_{AFE} Pbc_a$ phase after fatigue process. **a** Cross-section HAADF image of the TiN/HZO/TiN device after fatigue at $V_a = \pm 2.5$ V, $f = 500$ kHz, for 10^7 times. The image shows an O-phase grain projected along [010] zone axis. **b** The corresponding ABF image of **a**, demonstrating clearly the off-center O_{II} atomic columns shifted along the [001] direction (green) and $[00\bar{1}]$ direction (purple) alternately, showing a Pbc_a dominated structure. **c** The magnified ABF image acquires from the green square area in **b**, and the arrows show the deviating direction of O_{II} atomic columns from the center of the four nearest Hf/Zr columns.

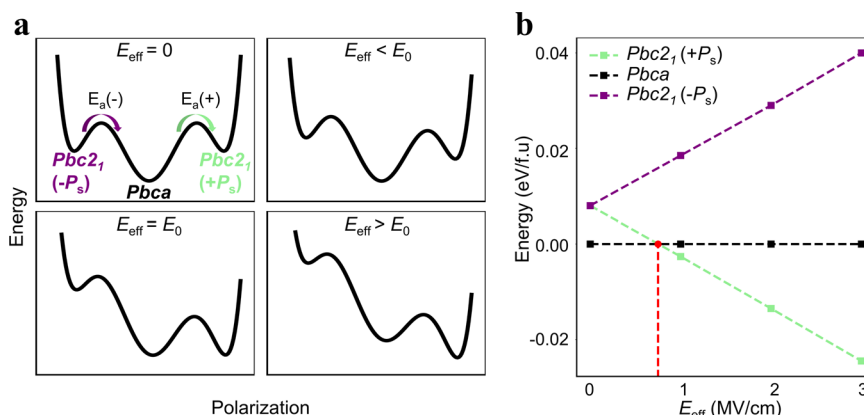


Fig. 5 Energy landscape and DFT calculations. **a** schematic diagrams of the energy landscape for the Pbc_a (center global minimum) and $Pbc2_1$ (two local minima at finite P) under zero E_{eff} and non-zero E_{eff} . **b** calculated energies of the Pbc_a , $Pbc2_1(-P_s)$, and $Pbc2_1(+P_s)$ as a function of E_{eff} .

Table 1 Effective field strength (E_{eff}) across the O_{FE} layer when the interfacial T-phase layer is present at V_a of 3, 4, and 5.5 V.

T-phase thickness (nm)	O_{FE} -phase thickness (nm)	E_{eff} (MV/cm) at $V_a = 3$ V	E_{eff} (MV/cm) at $V_a = 4$ V	E_{eff} (MV/cm) at $V_a = 5.5$ V	Note
0.75-1.00	14.25-14.00	0.83-0.76	1.16-1.11	1.67-1.62	Pristine
0.94-2.11	14.06-12.89	0.78-0.49	1.12-0.84	1.63-1.37	Woken-up
3.25-4.25	11.75-10.75	0.19--0.08	0.55-0.29	1.09-0.84	HF fatigue

Figure 5a shows the schematic diagrams of the energy landscape for Pbc_a (center global minimum) and $Pbc2_1$ (two local minima at finite P). Under the application of a negative E_{app} (more precisely, E_{eff}), the $-P_s$ and $+P_s$ (saturation polarization) states of the $Pbc2_1$ phase become more unstable and stable, respectively, while the nonpolar phase energy remained unchanged. When $E_{eff} > E_0$, the $Pbc2_1$ phase becomes energetically more favorable than the Pbc_a phase; this is summarized in Fig. 5b. The calculations showed that E_0 is ~ 0.8 MV/cm, i.e., when E_{eff} is lower or higher than 0.8 MV/cm, the $O_{AFE} Pbc_a$ phase or the $O_{FE} Pbc2_1$ phase becomes stable, respectively. The activation barrier (E_a) of the direct transition between $Pbc2_1$ and Pbc_a in HfO_2 was also calculated, which is directly related to the wake-up, fatigue, and rejuvenation. They are summarized with the calculated relative energy of $Pbc2_1$ to Pbc_a (ΔE), by ~ 10 meV/f.u., which is consistent with previous reports^{17,19} in Supplementary Table S1. Although the E_a depends on the transient path, i.e., the movement of O_{II} (off-center) atoms, these calculation results are comparable with previous studies, including the recent report by Xu et al.²⁹

Table 1 shows E_{eff} across the O_{FE} layer when the interfacial T-phase layer is present within the 0.75–1.0 nm range in the pristine state and in the 0.94–2.11 nm range in the woken-up state (the first and second rows). When V_a is 3 V or higher, E_{eff} was higher than E_0 for the pristine state, indicating that the film was prone to be woken-up, which is consistent with the results shown in Fig. 2c, except for the case where V_a is 3 V. This exception must be related to the still high activation barrier between the two phases (reaching as high as ~ 0.15 eV/f.u.), which prohibited fluent switching to the $Pbc2_1$ phase under this condition. In the woken-up sample case, E_{eff} became smaller because of the involvement of the higher depolarizing effect. Therefore, a V_a of at least ~ 4 V was necessary to keep the $Pbc2_1$ phase more stable than the Pbc_a phase during cycling. These calculation results strongly support the hypothesis for the wake-up and fatigue processes discussed in Figs. 1–4.

Finally, the structural variations and accompanying electrical performances after fatigue cycling with a V_a of ± 4 V are discussed. Supplementary Fig. S12a shows a STEM-HAADF image of the TiN/HZO/TiN capacitor after high- V_a fatigue testing (± 4 V, 10^8

cycles), which reduced the $2P_r$ value from 18.9 to 9.8 $\mu\text{C}/\text{cm}^2$ (Supplementary Fig. S13a). The corresponding STEM-ABF image along the [010] direction in Supplementary Fig. S12b clearly shows the alternating distributions of the O_{II} ion positions being shifted along the [001] (green) and $[00\bar{1}]$ (purple) directions. This finding demonstrates that high- V_a fatigue was also induced by the transition from the $\text{O}_{\text{FE}} \text{Pbc}2_1$ phase to the $\text{O}_{\text{AFE}} \text{Pbca}$ phase. Another notable finding from this sample is the development of a fairly thick interfacial T-phase, which can be seen in Supplementary Fig. S12a. The STEM-HAADF images of this high-field fatigued sample confirmed that the thickness of this layer was $\sim 3.25\text{--}4.25$ nm. The last row of Table 1 indicates that E_{eff} across the remaining $\sim 11.75\text{--}10.75$ nm-thick O_{FE} -phase is as low as 0.29–0.55 MV/cm for $V_a = 4$ V under these circumstances because of the severe depolarizing field effect. These calculation results thus corroborated the finding that high- V_a fatigue is induced by the transition from the $\text{Pbc}2_1$ phase to the Pbca phase and not by defect generation and the accompanying domain pinning.

Following the same line of reasoning used for rejuvenation of the low- V_a fatigued sample shown in Fig. 2f, a similar rejuvenation was attempted using $V_a = 5.5$ V that increased E_{eff} to $\sim 0.84\text{--}1.09$ MV/cm, as also shown in Table 1. Supplementary Fig. S13b shows the evolution of the P – V curve with increasing rejuvenation cycling numbers up to 10^4 . As expected, the fatigued sample is partly recovered. This is further strong evidence that the high- V_a fatigue was also induced by the phase transition mentioned above.

Similar electrical and structural characterizations were performed for the 5.6-nm-thick HZO film to prove the general applicability of the reversible phase transition model for the thinner films. The results are summarized in Supplementary Figs. S14–S21. Although the thinner film contained a higher portion of T-phase grains in the pristine state, in addition to the O-phase grains, it showed similar wake-up, fatigue, and rejuvenation processes. Therefore, it can be inferred that the reversible transition between the nonpolar Pbca phase and polar $\text{Pbc}2_1$ phase also occurs in the 5.6-nm-thick HZO film. The only difference is that the wake-up process in this thinner film is also contributed by the structural transition from the $\text{P}4_2/\text{nmc}$ T-phase to $\text{Pca}2_1$ O-phase.

The knowledge acquired based on the effects of the V_{O} concentration on the phase stability indicates that the increase in the interfacial T-phase thickness is reasonable; it has been reported previously that the highest V_{O} concentration stabilizes the T-phase over the O- and monoclinic (M)-phases^{28,30}. It must then be reasonable to believe that the repeated electrical stimuli enhanced the chemical interactions between the HZO film and the reactive TiN electrode, which would also increase the V_{O} concentration. It was also noted that these interfacial T-phases were mostly found around the top electrode interface. The bottom electrode interface was formed by depositing an HZO film on the TiN layer, which may produce a stable interface structure³¹. However, the top electrode interface was formed by depositing the TiN layer on the HZO film using a reactive sputtering process, which must have had a damaging effect on the HZO layer surface. Therefore, the top surface of the HZO layer must be vulnerable to oxygen concentration losses during electrical cycling tests.

Conclusion

The crystal structures of pristine, woken-up, fatigued, and rejuvenated O-phase grains in atomic layer-deposited ferroelectric HZO films were examined in detail using the Cs-corrected STEM-HAADF and STEM-ABF techniques. The results showed that the 180° domain boundary structure of the $\text{O}_{\text{FE}} \text{Pbc}2_1$ phase

is identical to the crystal structure of the $\text{O}_{\text{AFE}} \text{Pbca}$ phase, which is consistent with a previous theoretical expectation¹⁸. This structural relationship and the only slightly different energies of the two phases make the reversible phase change produced by the application of an electric field with a controlled magnitude feasible. The critical electric field for this transition was estimated to be ~ 0.8 MV/cm using DFT calculations.

The wake-up phenomenon could be induced by applying a voltage that exerted a switching field across the O_{FE} layer that was higher than the critical field. The interfacial T-phase grew as the number of switching cycles increased to the degree that was also dependent on the applied voltage. This interfacial T-phase generated a depolarizing field, which reduced the effective field applied to the remaining O_{FE} phase film. As the interfacial T-phase evolves in tandem with the increasing numbers of cycles, the effective field then becomes lower than the critical field, even at the given applied voltage; this is accompanied by the transition from wake-up to fatigue. However, because the fatigue in this material was not induced by irreversible defect generation and domain pinning but instead was induced by a (reversible) phase transition between the polar and antipolar phases, the fatigued sample could then be rejuvenated by applying a voltage that increased the effective field to exceed the critical field. This degradation mechanism for the ferroelectric performance of the HZO film is critically different from that of conventional perovskite-based FE thin films. A similar model can be applied to other fluorite-structured FE thin films, including variously doped HfO_2 films.

While the oxygen loss caused by the repeated electrical stimuli was the fundamental origin of the performance degradation, it did not affect the phase stability and FE performance of the O_{FE} phase film directly. Instead, the evolution of the interfacial T-phase caused the depolarization field effect over the remaining O_{FE} phase-based portion, which then promoted the transition to the ground state O_{AFE} phase. Therefore, preventing oxygen loss during repeated electrical operations remains the most crucial factor in achieving the ultimate performance levels when using these newly established FE films.

Methods

Device fabrication. The TiN/HZO/TiN capacitor fabrication processes were as follows. First, the TiN bottom electrodes were deposited on the SiO_2/Si substrate by ion beam sputtering. Then, 10–15-nm-thick HZO thin films were deposited by ALD at 280 °C. $\text{Hf}[\text{N}(\text{C}_2\text{H}_5)\text{CH}_3]_4$, $\text{Zr}[\text{N}(\text{C}_2\text{H}_5)\text{CH}_3]_4$, and H_2O were used as the Hf precursor, the Zr precursor, and the oxygen source, respectively. The Hf:Zr ratio was controlled by alternating deposition of one cycle of HfO_2 and one cycle of ZrO_2 . Also, 10-nm-thick nanolaminated $\text{HfO}_2/\text{ZrO}_2$ film, where each layer's thickness was 1 nm, was prepared. Subsequently, the top electrode (TiN) layer was sputtered and patterned into different sizes. Finally, the as-fabricated TiN/HZO/TiN ferroelectric capacitors were annealed for 30 s at 500 °C in a nitrogen atmosphere to crystallize the HZO.

Electrical measurements. The polarization–voltage (P – V) and leakage current characteristics of the metal-FE-metal devices were measured using a Radiant Workstation ferroelectric tester and an Agilent B1500 semiconductor parameter analyzer. During all electrical measurements, a bias voltage was applied to the bottom electrode, and the top electrode was grounded. The capacitor size was $100 \mu\text{m} \times 100 \mu\text{m}$.

Cs-STEM experiment. After the different electrical operations, the TiN/HZO/TiN capacitors were processed into cross-sectional samples using the focused ion beam (FIB) technique in the FEI Helios G4 system, including low-pressure polishing processes at 5 and 2 keV. The sample was treated in a Gatan 691 precision ion polishing system at 1–0.5 keV to remove any residual contamination and damage from the sample surface. The STEM experiments were then conducted on a JEM Grand ARM 300F microscope operating at 300 kV in the STEM mode with a probe aberration corrector. The HAADF and ABF images were acquired at a probe convergence semi-angle of ~ 18 mrad. The STEM-HAADF images were acquired using an annular dark-field image detector with an inner semi-angle of more than 64 mrad. The STEM-ABF images were acquired using a bright-field image detector

with its central section blocked using a beam stopper; the collection semi-angle was in the 12–24 mrad range.

DFT calculations. Ab initio calculations were performed using the Vienna Ab-initio Simulation Package (VASP)^{32,33}. The generalized gradient approximation of the Perdew–Burke–Ernzerhof (GGA-PBE) exchange–correlation functional³⁴ and Blöchl’s projector augmented wave (PAW) approach^{35,36} were used with an energy cut-off of 600 eV. The *k*-points were sampled and found to be $8 \times 8 \times 8$ for the *Pbc*2₁ unit cell and $8 \times 4 \times 8$ for the *Pbca* unit cell. The dielectric constant was obtained via density functional perturbation theory (DFPT)^{37,38}, and the spontaneous polarization was calculated using the Berry phase method³⁹. The activation barrier (E_a) for switching was estimated using the solid-state nudged elastic band (SS-NEB) method⁴⁰.

Reporting summary. Further information on research design is available in the Nature Research Reporting Summary linked to this article.

Received: 29 November 2021; Accepted: 12 January 2022;

Published online: 03 February 2022

References

- Park, M. H. et al. Ferroelectricity and antiferroelectricity of doped thin HfO₂-based films. *Adv. Mater.* **27**, 1811–1831 (2015).
- Mikolajick, T., Slesazek, S., Park, M. H. & Schroeder, U. Ferroelectric hafnium oxide for ferroelectric random-access memories and ferroelectric field-effect transistors. *MRS Bull.* **43**, 340–346 (2018).
- Park, M. H., Lee, Y. H., Mikolajick, T., Schroeder, U. & Hwang, C. S. Review and perspective on ferroelectric HfO₂-based thin films for memory applications. *MRS Commun.* **8**, 795–808 (2018).
- Muller, J., Polakowski, P., Mueller, S. & Mikolajick, T. Ferroelectric hafnium oxide based materials and devices: assessment of current status and future prospects. *ECS J. Solid State Sci. Technol.* **4**, N30–N35 (2015).
- Scott, J. F. & Dawber, M. Oxygen-vacancy ordering as a fatigue mechanism in perovskite ferroelectrics. *Appl. Phys. Lett.* **76**, 3801–3803 (2000).
- Warren, W. L. et al. Polarization suppression in Pb(Zr,Ti)O₃ thin films. *J. Appl. Phys.* **77**, 6695–6702 (1995).
- Li, L., Xie, L. & Pan, X. Real-time studies of ferroelectric domain switching: a review. *Rep. Prog. Phys.* **82**, 126502 (2019).
- Boescke, T. S., Muller, J., Brauhaus, D., Schroeder, U. & Bottger, U. Ferroelectricity in hafnium oxide thin films. *Appl. Phys. Lett.* **99**, 102903 (2011).
- Park, M. H. et al. Toward a multifunctional monolithic device based on pyroelectricity and the electrocaloric effect of thin antiferroelectric Hf_{1-x}Zr_xO₂ films. *Nano Energy* **12**, 131–140 (2015).
- Park, M. H. et al. Thin Hf_xZr_{1-x}O₂ films: a new lead-free system for electrostatic supercapacitors with large energy storage density and robust thermal stability. *Adv. Energy Mater.* **4**, 1400610 (2014).
- Park, M. H. & Hwang, C. S. Fluorite-structure antiferroelectrics. *Rep. Prog. Phys.* **82**, 124502 (2019).
- Zhou, D. Y. et al. Wake-up effects in Si-doped hafnium oxide ferroelectric thin films. *Appl. Phys. Lett.* **103**, 192904 (2013).
- Kim, H. J. et al. A study on the wake-up effect of ferroelectric Hf_{0.5}Zr_{0.5}O₂ films by pulse-switching measurement. *Nanoscale* **8**, 1383–1389 (2016).
- Park, M. H. et al. Effect of Zr content on the wake-up effect in Hf_{1-x}Zr_xO₂ films. *ACS Appl. Mater. Interfaces* **8**, 15466–15475 (2016).
- Pescic, M. et al. Physical mechanisms behind the field-cycling behavior of HfO₂-based ferroelectric capacitors. *Adv. Funct. Mater.* **26**, 4601–4612 (2016).
- Grimley, E. D. et al. Structural changes underlying field-cycling phenomena in ferroelectric HfO₂ thin films. *Adv. Electron. Mater.* **2**, 1600173 (2016).
- Materlik, R., Kuenneth, C. & Kersch, A. The origin of ferroelectricity in Hf_{1-x}Zr_xO₂: a computational investigation and a surface energy model. *J. Appl. Phys.* **117**, 134109 (2015).
- Lee, H.-J. et al. Scale-free ferroelectricity induced by flat phonon bands in HfO₂. *Science* **369**, 1343–1347 (2020).
- Batra, R., Huan, T. D., Rossetti, G. A. & Ramprasad, R. Dopants promoting ferroelectricity in Hafnia: insights from a comprehensive chemical space exploration. *Chem. Mater.* **29**, 9102–9109 (2017).
- Findlay, S. et al. Dynamics of annular bright field imaging in scanning transmission electron microscopy. *Ultramicroscopy* **110**, 903–923 (2010).
- Ohtaka, O. et al. Phase relations and equations of state of ZrO₂ under high temperature and high pressure. *Phys. Rev. B* **63**, 174108 (2001).
- Ohtaka, O. et al. Phase relations and volume changes of hafnia under high pressure and high temperature. *J. Am. Ceram. Soc.* **84**, 1369–1373 (2001).
- Park, M. H. et al. Surface and grain boundary energy as the key enabler of ferroelectricity in nanoscale hafnia-zirconia: a comparison of model and experiment. *Nanoscale* **9**, 9973–9986 (2017).
- Park, M. H. et al. Understanding the formation of the metastable ferroelectric phase in hafnia-zirconia solid solution thin films. *Nanoscale* **10**, 716–725 (2018).
- Park, M. H., Lee, Y. H. & Hwang, C. S. Understanding ferroelectric phase formation in doped HfO₂ thin films based on classical nucleation theory. *Nanoscale* **11**, 19477–19487 (2019).
- Park, M. H., Lee, Y. H., Mikolajick, T., Schroeder, U. & Hwang, C. S. Thermodynamic and kinetic origins of ferroelectricity in fluorite structure oxides. *Adv. Electron. Mater.* **5**, 1800522 (2019).
- Schenk, T. et al. Complex internal bias fields in ferroelectric hafnium oxide. *ACS Appl. Mater. Interfaces* **7**, 20224–20233 (2015).
- Schenk, T. et al. Electric field cycling behavior of ferroelectric hafnium oxide. *ACS Appl. Mater. Interfaces* **6**, 19744–19751 (2014).
- Xu, X. et al. Kinetically stabilized ferroelectricity in bulk single-crystalline HfO₂:Y. *Nat. Mater.* **20**, 826–832 (2021).
- Hoffmann, M. et al. Stabilizing the ferroelectric phase in doped hafnium oxide. *J. Appl. Phys.* **118**, 072006 (2015).
- Weinreich, W. et al. Impact of interface variations on J–V and C–V polarity asymmetry of MIM capacitors with amorphous and crystalline Zr_(1-x)Al_xO₂ films. *Microelectron. Eng.* **86**, 1826–1829 (2009).
- Kresse, G. & Furthmüller, J. Efficiency of ab-initio total energy calculations for metals and semiconductors using a plane-wave basis set. *Comput. Mater. Sci.* **6**, 15–50 (1996).
- Kresse, G. & Furthmüller, J. Efficient iterative schemes for ab initio total-energy calculations using a plane-wave basis set. *Phys. Rev. B* **54**, 11169–11186 (1996).
- Perdew, J. P., Burke, K. & Ernzerhof, M. Generalized gradient approximation made simple. *Phys. Rev. Lett.* **77**, 3865–3868 (1996).
- Blöchl, P. E. Projector augmented-wave method. *Phys. Rev. B* **50**, 17953 (1994).
- Kresse, G. & Joubert, D. From ultrasoft pseudopotentials to the projector augmented wave method. *Phys. Rev. B* **59**, 1758–1775 (1999).
- Gonze, X. & Lee, C. Dynamical matrices, born effective charges, dielectric permittivity tensors, and interatomic force constants from density-functional perturbation theory. *Phys. Rev. B* **55**, 10355–10368 (1997).
- Baroni, S., De Gironcoli, S., Dal Corso, A. & Giannozzi, P. Phonons and related crystal properties from density-functional perturbation theory. *Rev. Mod. Phys.* **73**, 515–562 (2001).
- King-Smith, R. & Vanderbilt, D. Theory of polarization of crystalline solids. *Phys. Rev. B* **47**, 1651–1654 (1993).
- Henkelman, G., Uberuaga, B. P. & Jónsson, H. A climbing image nudged elastic band method for finding saddle points and minimum energy paths. *J. Chem. Phys.* **113**, 9901–9904 (2000).

Acknowledgements

We thank the valuable discussion from Prof. C. Ge at the Institute of Physics, Chinese Academy of Sciences, Prof. A.Q. Jiang with Fudan University, and Prof. B. Chen with Zhejiang University. H. Lyu was supported by the National Natural Science Foundation of China under Grants 61834009, 62025406 and the Strategic Priority Research Program of the Chinese Academy of Sciences under Grant No. XDB44010300. J.-H. Choi was supported by the National Research Foundation of Korea (NRF) grant funded by MSIT [2020R1A2C2003931], and by the Institutional Research Program of the Korea Institute of Science and Technology (KIST) [2E31221]. C.S. Hwang was supported by the National Research Foundation of Korea (2020R1A3B2079882). Y. Cheng was supported by the National Natural Science Foundation of China (92064003, 62174054, 62104071, 12134003), and the Shanghai Sailing Program (21YF1410900). We thank David MacDonald, MSc, from Liwen Bianji, Edanz Editing China (www.liwenbianji.cn/ac), for editing the English text of a draft of this manuscript.

Author contributions

Y.C., Z.G., C.S.H., and H.L. designed the experiments. Z.G. and J.G. carried out sample fabrication. Z.G. and H.L. carried out electrical experiments. Y.C., Y.H.Z., and Y.Z.Z. carried out the STEM measurement and result analysis. H.W.P., M.H.P., K.H.Y., and J.-H.C. proposed the model and did the theoretical calculation. J.G. and K.-H.X. provided help on data analysis and discussion. H.L., Y.C., J.-H.C., and C.S.H. wrote the paper. C.S.H. and H.L. supervised the research.

Competing interests

The authors declare no competing interests.

Additional information

Supplementary information The online version contains supplementary material available at <https://doi.org/10.1038/s41467-022-28236-5>.

Correspondence and requests for materials should be addressed to Cheol Seong Hwang or Hangbing Lyu.

Peer review information *Nature Communications* thanks other anonymous reviewer(s) for their contribution to the peer review of this work. Peer reviewer reports are available.

Reprints and permission information is available at <http://www.nature.com/reprints>

Publisher's note Springer Nature remains neutral with regard to jurisdictional claims in published maps and institutional affiliations.



Open Access This article is licensed under a Creative Commons Attribution 4.0 International License, which permits use, sharing, adaptation, distribution and reproduction in any medium or format, as long as you give appropriate credit to the original author(s) and the source, provide a link to the Creative Commons license, and indicate if changes were made. The images or other third party material in this article are included in the article's Creative Commons license, unless indicated otherwise in a credit line to the material. If material is not included in the article's Creative Commons license and your intended use is not permitted by statutory regulation or exceeds the permitted use, you will need to obtain permission directly from the copyright holder. To view a copy of this license, visit <http://creativecommons.org/licenses/by/4.0/>.

© The Author(s) 2022